Inorganic Chemistry

Article

pubs.acs.org/IC

Polarization Dependent High Energy Resolution X-ray Absorption Study of Dicesium Uranyl Tetrachloride

Tonya Vitova,*,[†] Jennifer C. Green,[‡] Robert G. Denning,[‡] Matthias Löble,[†] Kristina Kvashnina,[§] Joshua J. Kas,[∥] Kevin Jorissen,[∥] John J. Rehr,[∥] Thomas Malcherek,[⊥] and Melissa A. Denecke[†,△]

[†]Karlsruhe Institute of Technology, Institute for Nuclear Waste Disposal, P.O. Box 3640, 76021 Karlsruhe, Germany

[‡]Department of Chemistry, Oxford University, South Parks Road, Oxford OX1 3QR, U.K.

[§]European Synchrotron Radiation Facility (ESRF), 6 Rue Jules Horowitz, BP 220, 38043 Grenoble Cedex 9, France

[∥]Department of Physics, University of Washington, Seattle, Washington 98195, United States

[⊥]Department of Geosciences, University of Hamburg, Grindelallee 48, 20146 Hamburg, Germany

Ⓢ *Supporting Information*

ABSTRACT: Dicesium uranyl tetrachloride ($Cs_2UO_2Cl_4$) has been a model compound for experimental and theoretical studies of electronic structure of U(VI) in the form of UO_2^{2+} (uranyl ion) for decades. We have obtained angle-resolved electronic structure information for oriented $Cs_2UO_2Cl_4$ crystal, specifically relative energies of 5f and 6d valence orbitals probed with extraordinary energy resolution by polarization dependent high energy resolution X-ray absorption near edge structure (PD-HR-XANES) and compare these with predictions from quantum chemical Amsterdam density functional theory (ADF) and ab initio real space multiple-scattering Green's function based FEFF codes. The obtained results have fundamental value but also demonstrate an experimental approach, which offers great potential to benchmark and drive improvement in theoretical calculations of electronic structures of actinide elements.

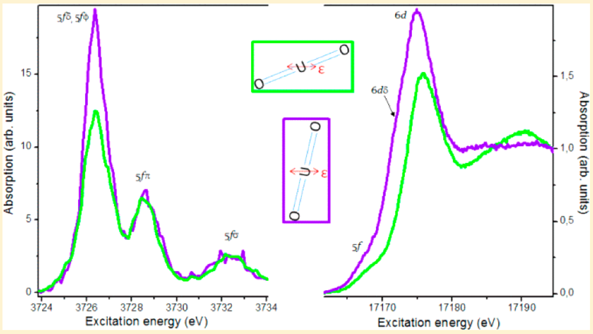

1. INTRODUCTION

The physics and chemistry of uranium plays a central role in the safety assessment of a nuclear waste repository and reduction of the radiotoxicity of spent nuclear fuel, which are of fundamental importance for safe and sustainable use of nuclear energy. Detailed knowledge about the U oxidation state and electronic structure is necessary to predict its reactivity, which determines U mobilization/immobilization behavior in the environment, for example, in case of water intrusion in a deep geological repository.[1] Furthermore, insight into actinide (An) electronic structure facilitates understanding and ultimately fine-tuning N-donor ligand selectivity for An over their chemically similar lanthanide (Ln) analogs necessary for separating An from Ln in a key step in the so-called partitioning and transmutation (P&T) strategy for reduction the radiotoxicity of spent nuclear fuel.[2] Despite numerous experimental and theoretical studies, the electronic structure of U(VI) (mostly present as the UO_2^{2+} uranyl ion) remains subject of discussion.[3−6]

The uranyl moiety is highly symmetric with linear structure with unusually short, strong covalent bonding to two axial O atoms. The linear structure leads to the U valence orbitals being most usefully described in terms of their σ, π, δ, or ϕ character with respect to rotation about the U−O z-axis. Introduction of four Cl groups along the x and y axes, giving D_{4h} symmetry, lifts the degeneracy of the δ symmetry orbitals. The residual doubly degenerate U orbitals when singly occupied experience strong spin−orbit coupling and the resultant orbital energy manifold needs inclusion of this effect to account for the ordering. The axial nature of the uranyl ion leads to anisotropic character and a strong polarization dependency of the uranyl X-ray absorption spectroscopy (XAS) signal.[7,8] In this study, the aim is to extend the current knowledge about the electronic structure of $UO_2Cl_4^{2-}$. The relative energies of the occupied and unoccupied $UO_2Cl_4^{2-}$ valence molecular orbitals with 5f and 6d character derived from optical experiments and XAS have been extensively reviewed and compared to scalar relativistic zeroth order regular approximation (ZORA) density functional theory (DFT) calculations employing the BP86 functional.[5,9] We compare the relative energies of the unoccupied $UO_2Cl_4^{2-}$ 5f- and 6d-based valence orbitals calculated with Amsterdam density functional theory (ADF)[10] code with those measured from experimental U L_3-edge high energy resolution polarization dependent X-ray absorption near edge structure (PD-HR-XANES) of a dicesium uranyl tetrachloride ($Cs_2UO_2Cl_4$) crystal grown along the b crystallographic axis (see Figure 1 bottom). Selective transitions to U 5f

Received: August 16, 2014
Published: December 8, 2014

dx.doi.org/10.1021/ic5020016 | *Inorg. Chem.* 2015, 54, 174−182

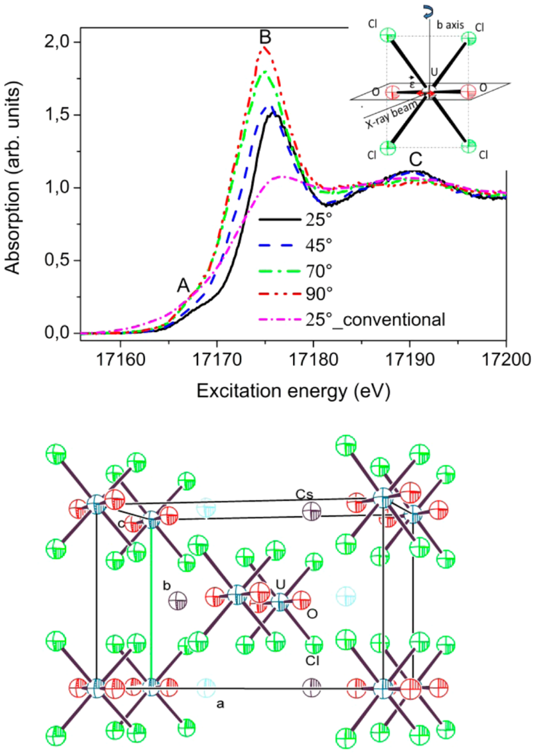

Figure 1. U L_3-edge PD-HR-XANES and a conventional PD-XANES of $Cs_2UO_2Cl_4$ (top) for different angles between the uranyl moiety UO_2^{2+} and the polarization vector of the incident X-ray beam ε (top, inset); the unit cell of $Cs_2UO_2Cl_4$ (bottom).

or 6d valence orbitals (U $2p_{3/2} \rightarrow 5f/6d$) are detected in the same U L_3-edge PD-HR-XANES spectrum with remarkable energy resolution. The experimental observations combined with theoretical results allow qualitative evaluation of the level of mixing of O, Cl, and U valence orbitals. The U L_3-edge PD-HR-XANES spectra are also successfully reproduced by ab initio real space multiple-scattering Green's function based theoretical FEFF9.6 code calculations.[11] The relative energy positions of U $3d_{3/2} \rightarrow 5f$ electronic transitions experimentally probed by U M_4-edge PD-HR-XANES are also discussed in comparison to the ADF results.

2. EXPERIMENTAL DETAILS

2.1. Preparation and Characterization of Dicesium Uranyl Tetrachloride ($Cs_2UO_2Cl_4$).[12] $Cs_2UO_2Cl_4$ was prepared from uranylacetate and cesium chloride. For the preparation of uranylacetate ($UO_2(CH_3CO_2)_2$) $UO_2(NO_3)_2$ (1 g, 2.5 mmol) was dissolved in water and heated to 100 °C. An excess of ammonium chloride (3 g) was added to the boiling solution and the pH-value adjusted with concentrated ammonia. Yellow flakes of ammonium-diuranate precipated after it was cooled to room temperature. After the overlaying solution was decanted, the yellow precipitate was washed with water several times (8−9 mL). The precipitate was then dried at 80−100 °C and the resulting product ground with mortar and pestle. The resulting yellow powder was calcined under ambient atmosphere at 350 °C for 12 h to obtain an oxide. The red product was suspended in water (30 mL), heated to 80 °C and dissolved in 10 mL concentrated acetic acid. The hot solution was filtered and the filtrate cooled down to room temperature. After standing overnight, yellow rod shaped crystals of $UO_2(CH_3COO)_2$ 2 H_2O were isolated. The crystals were washed with dilute acetic acid and dried at room temperature in air. (Yield: 634 mg, 1.6 mmol, 64%). Yellow crystalline $UO_2(CH_3COO)_2{\cdot}2H_2O$ (500 mg, 1.2 mmol) was dissolved in 10 mL of hot dilute HCl and a stochiometric amount of CsCl added. After cooling to room temperature, the pretcipitated product was isolated and recrystallized from dilute hydrochloric acid solution. The yellow crystalline $Cs_2UO_2Cl_4$, with rod crystallites grown along the b crystallographic axis (see Figure 1) were filtered and dried at room temperature in air (yield = 212 mg, 0.31 mmol, 25.8%).

Face indices of a selected $Cs_2UO_2Cl_4$ crystal were determined using single crystal X-ray diffraction (Nonius KappaCCD, graphite monochromated Mo Kα radiation). The obtained orientation matrix yields monoclinic lattice parameters a = 11.903 Å, b = 7.682 Å, c = 5.771 Å, β = 100.15°, V = 519.44 Å^3, Observed deviations from the lattice parameters reported in the Inorganic Crystal Structure Database (ICSD), entry 39490, a = 12.0058, b =7.6973, c =5.8503, β = 100.0°, V = 532.34 Å^3, space group C1m1, might be attributed to absorption effects caused by the large crystal size. These are of no significance for the results obtained for actual $Cs_2UO_2Cl_4$ crystal employed here.

2.2. XAS Experiments. The XAS experiments at the U L_3- (17166 eV), and M_4-edge (3728 eV) of a $Cs_2UO_2C_4$ crystal with approximate dimensions 0.5 × 0.5 × 5 mm were performed at the ID26 beamline at the European Synchrotron Radiation Facility (ESRF), Grenoble, France. The synchrotron radiation was monochromatized by a Si(311) (U L_3)/Si(111) (U M_4) double crystal monochromator (DCM). Rejection of higher harmonics was achieved by two Pd/Cr (U L_3)/Si (U M_4) mirrors working under total reflection. The energy calibration was performed assigning 17998/4966 eV to the first inflection point of a Zr K-edge (U L_3)/Ti K-edge (U M_4) XANES spectrum. All reported experiments were performed at room temperature.

U L_3-edge extended X-ray absorption fine structure (EXAFS) spectra were measured in fluorescence mode using an avalanche photodiode (APD).

During the PD-HR-XANES measurements for each excitation energy the U Lα_1 (13614 eV)/Mß (3339.8 eV) emission was selected by a spherically bent Ge(777)/Si(220) analyzer crystal and focused on an APD (U L_3)/single pixel silicon drift detector (SDD) KETEK (U M_4). The sample, crystal, and detector were positioned on a circle (Rowland geometry) with diameter 1 m equal to the bending radius of the crystal.[13] A combined incident convoluted with emitted energy resolution of 1.8 eV (U L_3)/0.8 eV(U M_4) was estimated by measuring the full width at half-maximum of the quasi-elastic peak. During the U M_4-edge experiments a polyethylene balloon filled with He and equipped with three 10 μm thick polyethylene windows was placed between sample, analyzer crystal, and detector to avoid absorption of low energy Mß fluorescence photons by air.

U L_3/M_4-edge PD-HR-XANES/U L_3-EXAFS measurements were performed for 25° (EXAFS), 45°, 70°, and 90° (EXAFS) (U L_3) and $\alpha = \alpha_1 + 5°$ ($0° \leq \alpha_1 \leq 45°$), α + 10°, α + 20°, α + 30°, and α + 40° (U M_4) orientation of the uranyl moiety UO_2^{2+} in the crystal with respect to the polarization vector ε of the primary beam (rotation around the b crystal axis, which corresponds to the long side of the crystal) (see Figure 1). For the U M_4-measurements the initial angle (α) between ε and UO_2^{2+} was not precisely determined; therefore a parameter α_1, which can have value within the interval $0° \leq \alpha_1 \leq 45°$ is introduced. The orientation notations are used in the manuscript. The energy of the incident beam was scanned from 17151.2/16785 to 17225.2/17853 eV with 0.1/1 eV step size, 600/100 s per HR-XANES/EXAFS spectrum, over the U L_3-edge and from 3715 to 3750 eV with 0.1 eV step size, 60 s per HR-XANES over the U M_4-edge. At least three spectra for each angle were collected in order to check the reproducibility of the spectral features and to improve the counting statistics. The measured spectra showed no occurrence of radiation damage.

U L_3-edge EXAFS measurement of a powder $Cs_2UO_2Cl_4$ sample is performed at the INE-Beamline for actinide research at ANKA synchrotron radiation facility, Karlsruhe, Germany. See the Supporting Information for experimental details and details on the analyses of all EXAFS data.

Linear combination least-squares (LCLS) fit analyses of the U L_3- and M_4-edge PD-HR-XANES spectra of $Cs_2UO_2Cl_4$ were performed with the WINXAS program (www.winxas.de) using three (U L_3) or five (U M_4) pseudo-Voigt (PV) [$f(x)$ = αGaussian + (1 −

α)Lorentzian] and one arctangent functions. The Levenberg–Marquardt least-squares algorithm is used in the fit.

2.3. Computational Details. *2.3.1. ADF.* The calculations presented in section 3.2 used the Amsterdam Density Functional program suite,[14] ADF2000.2.[15] An uncontracted triple-ζ basis set of Slater type orbitals was used with two additional polarization functions for O and Cl (ADF type V). Scalar relativistic corrections were included via the ZORA method.[16] All electrons were included. The local density parametrization of Vosko, Wilk, and Nusair[17] was employed, with exchange and correlation corrections as advocated by Becke in 1988,[18] and Perdew in 1986,[19] respectively. From the eigenvectors of a ADF calculation, we obtained the radial amplitude of the orbitals involved in the U L_3-edge PD-HR-XANES transitions (see Supporting Information Figure S1). Notice the very small amplitude of the 7s orbital in the region where that of $2p_{3/2}$ is large, and also the extensive cancellation where these functions overlap. As a result the $R^{(1)}_{2p/7s}$ integral is too small to provide significant intensity in XANES. The radial extent of the $2p_{3/2}$ shell is critical in the calculation of the transition moments so the characteristics of the orbitals obtained using an ADF calculation that includes the spin–orbit interaction, are compared with those from a full relativistic Hartree–Fock calculation, as tabulated by Desclaux. Excellent agreement is obtained for the average value of various powers of r, so the eigenfunctions from the ADF calculation were used with confidence for the calculation of the radial integrals.

2.3.2. FEFF9.6. The U L_3-edge $Cs_2UO_2Cl_4$ PD-HR-XANES spectra and the O, Cl, and U density of states were calculated with the FEFF9.6 ab initio quantum chemical code based on the multiple scattering theory.[11] The potentials of free atoms were calculated with a relativistic Dirac–Fock atom code part of FEFF9.6. The scattering potentials were calculated self-consistently by overlapping the free atomic density in the muffin thin approximation within a cluster of 149 atoms (SCF card). The UNFREEZEF card was used to include the U f states in the SCF calculation providing their accurate energy position.[20] The energy dependent exchange Hedin–Lundquist potential was used for the fine structure and the atomic background (EXCHANGE card). The Fermi energy was corrected by 2 eV to lower energies and the core-hole lifetime broadening was reduced by 2.5 eV leading to a broadening of 5.6 eV. The full multiple scattering XANES spectra were calculated for an atomic cluster of 228 atoms centered on the absorbing U atom (FMS and XANES cards). Best agreement between calculation and experiment was found by applying “COREHOLE RPA” option to screen the $2p_{5/2}$ core-hole. The orientation of the vector of polarization of the incident monochromatic radiation (ε) parallel or perpendicular to the UO_2^{2+} molecular axis was achieved by using the POLARIZATION card. The spectra were calculated for dipole or dipole and quadrupole electronic transitions (MULTIPOLE card). Note that “MULTIPOLE 2” in combination with the POLARIZATION card is only possible by using the ELLIPTICITY card depicting perpendicular orientation of ε with respect to the incident beam denoting linearly polarized incident X-ray beam (see Supporting Information).

3. RESULTS AND DISCUSSION

3.1. Experiment. The U L_3-edge PD-HR-XANES spectra of a $Cs_2UO_2Cl_4$ crystal for 25°, 45°, 70°, and 90° orientation of the uranyl moiety with respect to the linear polarization vector ε of the incident X-ray beam (inset in Figure 1) and conventionally measured PD-XANES for 25° are shown in Figure 1. The absorption resonances (A, B, C) of the PD-HR-XANES spectra are more resolved in energy compared to the 25° conventional PD-XANES as a result of reduced core-hole lifetime broadening effects.[21] An additional resonance A is detected and B and C resonances are well-separated in all PD-HR-XANES. The width narrowing of the U L_3-edge spectral features reduces uncertainties of energy positions, intensities and areas of the A, B and C features modeled by pseudo-Voigt (PV) profiles (see Figure 2, Table 1). The observed pre-edge feature A, previously assigned to $2p_{3/2} \rightarrow 5f$ quadrupole allowed electronic transitions for U(VI) materials,[22] shifts by −1.5 eV ± 0.1 eV to lower energy for the 90° compared to the 25° spectrum. The most pronounced absorption resonance B (white line, WL) describes dipole allowed $2p_{3/2} \rightarrow 6d$ electronic transitions. Previous conventional PD-XAS studies of a $RbUO_2(NO_3)_3$ single crystal reports predominant transitions to 6dδ and 6dπ orbitals in this spectral area for 90° and 0° orientation, respectively.[5,9] In Figure 1, the WL shifts −0.9 ± 0.1 eV to lower energies and its integral intensity increases going from the 25° to the 90° spectrum.

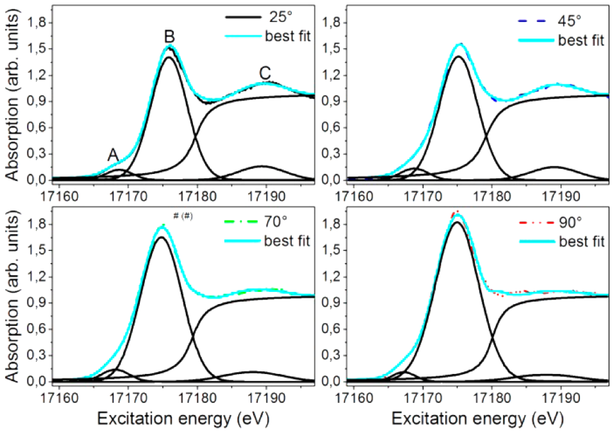

Figure 2. U L_3-edge PD-HR-XANES spectra and fits of $Cs_2UO_2Cl_4$; three PV and an arctangent functions used in the LCLS fit analyses (see Table 1).

The postedge absorption resonance C gains intensity and area approaching a 0° angle between linear UO_2^{2+} units and ε due to an increasing contribution of photoelectron multiple scattering along O axial atoms.[7,8]

The U M_4-edge PD-HR-XANES spectra measured for angles $\alpha = \alpha_1 + 5°$ $(0° \leq \alpha_1 \leq 45°)$, $\alpha + 10°$, $\alpha + 20°$, $\alpha + 30°$, and $\alpha + 40°$ orientation of the uranyl moiety with respect to ε of the incident X-ray beam are shown in Figure 3. The absorption resonance marked E is not resolved in the conventional U M_4-edge XANES spectrum.[20,23,24]

The M_4-edge $3d_{3/2} \rightarrow 5f$ electronic transitions probe unoccupied orbitals with predominant U 5f character. Previously performed DFT calculations suggest that the first intense peak D describes transitions to U 5fδ and 5fϕ orbitals.[5,9,24] Peaks E and F are shifted by 2.2 ± 0.1 and 6 ± 0.1 eV to higher energy compared to peak D (see Figure 4 and Table 2) and probe U 5fπ and 5fσ orbitals, respectively.[5,9,24] It was estimated from optical spectroscopy data that 5fδ and 5fϕ should be separated by about 0.3 eV,[5] whereas about 0.6 eV energy difference is resolved in our experimental data, manifested by an asymmetric shape of the D peak in the U M_4-edge PD-HR-XANES $\alpha = \alpha_1 + 5°$ $(0° \leq \alpha_1 \leq 45°)$ spectrum (see Supporting Information Figure S5). $5f\delta_{3/2}$ and $5f\phi_{3/2}$ are nearly degenerate as well as $5f\delta_{5/2}$ and $5f\phi_{7/2}$ (see Table 4 and Figure 5). The 5fπ orbital should be shifted by about 2.2 eV from 5fδ and 5fϕ and this agrees with our experimental observations.[4,5] O K-edge XANES results report about 2.7 eV energy difference between the U 5fσ and 5fπ orbitals,[5,9] whereas we find about 3.8 eV (see Figure 4 and Table 2). The discrepancy of about 1 eV might be attributed to different screening of the O 1s core-hole in the O K-edge XANES compared to the U $3d_{3/2}$ core-hole in the U M_4-edge PD-HR-XANES. The U 5fδ and 5fϕ orbitals are nonbonding

Table 1. Name of Spectrum and Absorption Feature, Height, Position, and Full Width at Half Maximum (FWHM) Parameters of the PV Functions Used to Model the U L_3-edge PD-HR-XANES Spectra and an Arctangent Used to Model the Edge Jump, the Gauss Part (Gauss Part α) and the Area of the PV Profiles, and the Residual between Experimental Data and Best Fit

spectrum	feature	height ± 0.01	position ± 0.1 (eV)	fwhm ± 0.1 (eV)	gauss part α	area of PV	residual (%)
25°	A	0.12	17168.7	4.7	1[a]	0.6	2.6
45°	A	0.13	17168.8	4.8	1[a]	0.7	1.7
70°	A	0.14	17168.1	4.7	1[a]	0.7	1.8
90°	A	0.11	17167.2	4.0	1[a]	0.5	2.1
25°	B	1.41	17175.9	6.3	1[a]	9.5	2.6
45°	B	1.41	17175.2	6.6	1[a]	9.9	1.7
70°	B	1.65	17174.8	7.0	1[a]	12.4	1.8
90°	B	1.82	17175.0	7.5	1[a]	14.7	2.1
25°	C	0.16	17189.4	8.0	1[a]	1.3	2.6
45°	C	0.15	17189.1	8.1	1[a]	1.3	1.7
70°	C	0.11	17188.1	10.2	1[a]	1.2	1.8
90°	C	0.08	17187.9	11.3	1[a]	0.9	2.1
25°	arctan	1[a]	17179.8	5.3		18.4	2.6
45°	arctan	1[a]	17179.2	5.6		18.1	1.7
70°	arctan	1[a]	17179.3	5.0		19.5	1.8
90°	arctan	1[a]	17180.1	4.2		16.8	2.1

[a] The parameter is fixed during the fit.

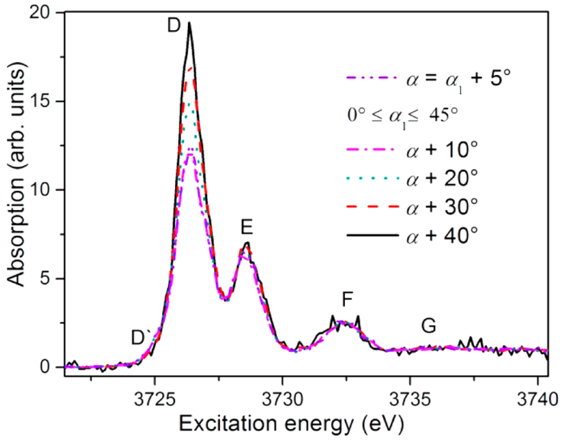

Figure 3. U M4-edge PD-HR-XANES spectra for different angles between the uranyl moiety UO_2^{2+} and the polarization vector of the incident X-ray beam ε.

with respect to O with dominating 5*f* character.[4,5] There is experimental and theoretical evidence for a relatively larger 5*fσ* contribution to the U−O bond than of the 5*fπ* orbital, mainly because of hybridization of the former with the 6*pσ* orbital.[9] Results from Cl K-edge XANES and DFT calculations report that up to 8% Cl 3*p* character is mixed with the U 5*fδ*, 5*fϕ* and 5*fπ* orbitals.[6]

Polarization dependence is manifested mainly by a decrease in area of the first intense absorption resonance D in case of $\alpha = \alpha_1 + 5°$ ($0° \leq \alpha_1 \leq 45°$), compared to the α + 40° geometry (see Figure 3). The energy positions of the D′, D, E, F, and G features are not observed to be a function of ε within the sensitivity of the measurements. No significant variations of peak area for resonant features D′, E, and F is detected, as α changes only by 40°. Such variations are demonstrated for 90° and 0° geometries in quantum chemical calculations of U M_5-edge PD-XANES of $UO_2(NO_3)_2{\cdot}6H_2O$.[24]

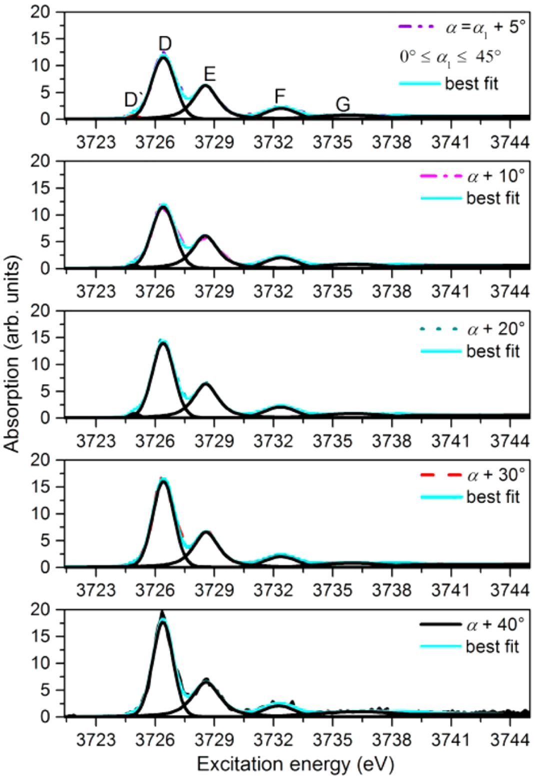

Figure 4. U M4-edge PD-HR-XANES spectra and fits of $Cs_2UO_2Cl_4$; five PV and an arctangent functions used in the LCLS fit analyses (see Table 2).

3.2. ZORA ADF Calculations. To simulate the U L_3-edge PD-HR-XANES spectra, the relative energies of the various excited states are required. Figure 5 illustrates the steps in the procedure for approximating these by means of a series of DFT calculations. The *z*-axis corresponds to the 4-fold axis along the U−O bonds and the four Cl atoms lie on the x and y axes. Table 3 shows the relabeling of orbitals upon reducing symmetry from $D_{\infty h}$ to D_{4h} and inclusion of spin−orbit coupling. The first column shows the virtual self-consistent field (SCF) orbital energies for the electronic ground state of $UO_2Cl_4^{2-}$, relative to that of the highest occupied molecular orbital (HOMO), obtained using the ZORA that accounts for scalar relativistic effects (Darwin and mass-velocity corrections)

Table 2. Name of Spectrum and Absorption Feature, Height, Position, and Full Width at Half Maximum (FWHM) Parameters of the PV Functions Used to Model the U M_4 Edge PD-HR-XANES Spectra and an Arctangent Used to Model the Edge Jump, the Gauss Part (Gauss Part α) and the Area of the PV Profiles, and the Residual between Experimental Data and Best Fit

spectrum	feature	height ± 0.01	position ± 0.1 (eV)	fwhm ± 0.1 (eV)	gauss part α	area of PV	residual (%)
α + 40°	D′	0.42	3724.9	0.6	1^a	0.27	13.2
α + 30°	D′	0.46	3724.9	0.5	1^a	0.25	6.4
α + 20°	D′	0.86	3725.0	0.6	1^a	0.57	5.1
α + 10°	D′	0.68	3724.9	0.6	1.0 ± 0.05	0.45	4.9
$\alpha = \alpha_1 + 5°$	D′	0.73	3724.9	0.6	1^a	0.45	6.6
α + 40°	D	17.77	3726.4	1.2	0.93^a	23.5	13.2
α + 30°	D	16.06	3726.4	1.3	0.93^a	22.4	6.4
α + 20°	D	13.98	3726.4	1.3	0.93^a	20.0	5.1
α + 10°	D	11.51	3726.4	1.4	0.93 ± 0.01	17.4	4.9
$\alpha = \alpha_1 + 5°$	D	11.54	3726.4	1.4	0.93^a	17.6	6.6
α + 40°	E	6.49	3728.6	1.7	0.3^a	14.8	13.2
α + 30°	E	6.63	3728.6	1.5	0.3^a	13.8	6.4
α + 20°	E	6.38	3728.6	1.5	0.3^a	13.1	5.1
α + 10°	E	6.12	3728.5	1.5	0.29 ± 0.01	12.9	4.9
$\alpha = \alpha_1 + 5°$	E	6.30	3728.5	1.5	0.3^a	12.9	6.6
α + 40°	F	2.08	3732.3	1.9	1^a	4.2	13.2
α + 30°	F	2.02	3732.4	2.0	1^a	4.2	6.4
α + 20°	F	2.05	3732.4	2.0	1^a	4.3	5.1
α + 10°	F	2.03	3732.4	2.0	1.0 ± 0.02	4.2	4.9
$\alpha = \alpha_1 + 5°$	F	2.03	3732.4	1.9	1^a	4.0	6.6
α + 40°	G	0.98	3736.3	5.7	0.94^a	3.8	13.2
α + 30°	G	0.81	3736.0	4.2	0.94^a	3.7	6.4
α + 20°	G	0.82	3736.0	4.4	0.94^a	3.9	5.1
α + 10°	G	0.79	3736.0	4.4	0.94 ± 0.02	3.8	4.9
$\alpha = \alpha_1 + 5°$	G	0.78	3735.8	4.5	0.94^a	3.8	6.6
α + 40°	arctan	0.60^a	3738.0^a	1.4^a		7.0	13.2
α + 30°	arctan	0.60^a	3738.0^a	1.4^a		6.8	6.4
α + 20°	arctan	0.60^a	3738.0^a	1.4^a		6.8	5.1
α + 10°	arctan	0.57 ± 0.01	3738.03 ± 0.01	1.44 ± 0.01		7.0	4.9
$\alpha = \alpha_1 + 5°$	arctan	0.60^a	3738.0^a	1.4^a		7.0	6.6

[a] Parameter is fixed during the fit.

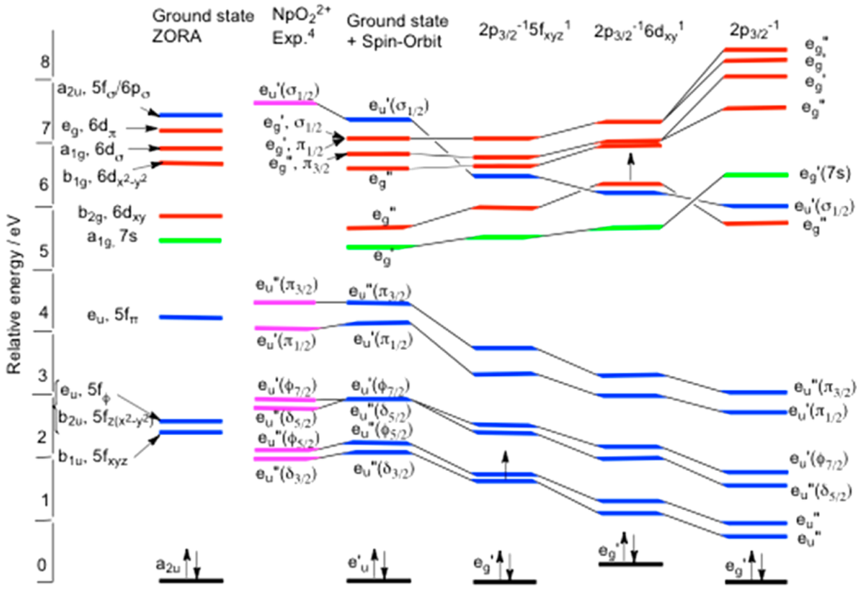

Figure 5. Theoretical SCF valence orbital energies showing the 6d orbitals (red), 5f (blue), and 7s (green) and their occupancy. The columns represent, from left to right, the ground state of $UO_2Cl_4^{2-}$ with scalar relativistic effects, the energy levels of NpO_2^{2+} from **4**, the ground state of $UO_2Cl_4^{2-}$ with spin−orbit coupling included, the levels of $UO_2Cl_4^{2-}$ with a 2p to 5f excitation, the levels of $UO_2Cl_4^{2-}$ with a 2p to 6d excitation and the levels of $UO_2Cl_4^{1-}$ with a 2p electron ionized. The orbital labels are correlated in Table 3.

Table 3. Irreducible Representations for Atomic Orbitals in the $D_{\infty h}$, D_{4h}, and D'_{4h} Double Group[a]

	s	p_x, p_y	p_z	d_{z^2}	d_{xz}, d_{yz}	d_{xy}	$d_{x^2-y^2}$	f_{z^3}	f_{xz^2}, f_{yz^2}	f_{xyz}	$f_{z(x^2-y^2)}$	$f_{x(x^2-3y^2)}$, $f_{y(3x^2-y^2)}$
$D_{\infty h}$	σ_g^+	π_u	σ_u^+	σ_g^+	π_g	δ_g		σ_u^+	π_u	δ_u		ϕ_u
D_{4h}	a_{1g}	e_u	a_{2u}	a_{ig}	e_g	b_{2g}	b_{1g}	a_{2u}	e_u	b_{1u}	b_{2u}	e_u
D'_{4h}(SO)	e'_g	e''_u, e'_u	e'_u	e'_g	e''_g, e'_g	e''_g	e''_g	e'_u	e''_u, e'_u	e''_u	e''_u	e''_u, e'_u

[a]NB the degeneracy of the δ symmetry orbitals is lifted shifting from linear to four-fold symmetry.

Table 4. Energies and Relative Intensities (F_D = dipole, F_Q = Quadrupole) of the Transitions to the Various Virtual Spinors[a]

spinor	$5f\delta_{3/2}$	$5f\phi_{5/2}$	$5f\delta_{5/2}$	$5f\phi_{7/2}$	$5f\pi_{1/2}$	$5f\pi_{3/2}$	$5f\sigma$	$6d_{xy}$	$6d_{x^2-y^2}$	$6d\pi_{1/2}$	$6d_{z^2}$	$6d\pi_{3/2}$
rel. energy/eV $(2p_{3/2})^{-1}$ $(5f/6d)^1$	0	0.08	0.81	0.92	1.77	2.15	4.95	5.21	5.89	5.89	6.22	6.22
rel. energy/eV $(2p_{3/2})^{-1}$	0	0.22	0.84	0.99	1.97	2.31	4.98	4.98	7.03	7.45	7.64	7.74
rel. intensity	14.3	14.3	14.3	14.3	14.3	14.3	14.3	576	576	576	576	576
F_Q (perpendicular, 90°)	2.50	7.50	2.50	7.50	0.50	0.50	0.00					
F_Q (parallel, 0°)	5.00	0.00	5.00	0.00	4.00	4.00	3.00					
F_D (perpendicular, 90°)								3.00	3.00	1.50	1.00	1.50
F_D (parallel, 0°)								0.00	0.00	3.00	4.00	3.00

[a]"Perpendicular, 90°" and "parallel, 0°" refer to perpendicular and parallel relation between uranyl cation and ε, respectively.

but excludes the spin–orbit interaction. The third column shows modifications introduced by the spin–orbit interaction and, in particular, the first order splitting of degenerate states with angular momentum about the O–U–O axis. These are quite small and the resulting 5f-electron levels are in satisfactory agreement with the f–f optical excitation energies observed in the $NpO_2Cl_4^{2-}$ ion[4] (second column). In addition, a core hole in an element has a similar effect on its valence levels as increasing the nuclear charge by one. Hence U with a core hole would be expected to have valence levels like Np. In the Np(V) system the spin–orbit splittings are somewhat larger, as one would expect for a metal with an additional nuclear charge, (cf., empirical coupling constants from optical spectra, i.e., ζ_U = 1855 cm^{-1} and ζ_{Np} = 2178 cm^{-1}[4]). The final three columns give virtual SCF orbital energies for configurations in which there is a hole in the $2p_{3/2}$ shell and in which the valence electron is located in either the $5f_{xyz}$ or the $6d_{xy}$ orbitals or has been completely ionized. The main effect of the core hole is to stabilize the 5f orbitals relative to the 6d; this is clearly visible in the fully ionized case (right-hand column). This, in turn, influences the nature of the HOMO, which changes from e'_u to e'_g symmetry due to the 5f and 6d content of these ligand-based spinors. The relative stabilization of the 5f shell is, however, less pronounced when the excited electron is retained in a 5f orbital than when it occupies a 6d orbital; evidently the 5f electron screens the core hole more effectively than the penetrating 6d orbital, as might be anticipated from the distribution of their amplitudes in the core region (see Supporting Information Figure S1). The nonbonding components of these shells illustrate this effect most clearly, since their orbital composition is found to be largely independent of the presence or absence of a core hole. When the excited electron remains bound ($2p_{3/2}^{-1}5f_{xyz}^1$ and $2p_{3/2}^{-1}6d_{xy}^1$ in Figure 5), the relative energies of the various components within the 5f manifold and within the 6d manifold are essentially independent of the nature of the configuration. In contrast, in the fully ionized case (far right column) there is a striking increase of the tetragonal field splitting of the $6d_{xy}$ and $6d_{x^2-y^2}$. This presumably results from the $6d_{x^2-y^2}$ orbital becoming strongly σ-antibonding when its absolute energy (along with the other metal-based MOs) is lowered relative to that of the equatorial chloride ligands.

The total SCF energies of the $2p_{3/2}^{-1}5f_{xyz}^1$, and $2p_{3/2}^{-1}6d_{xy}^1$ configurations are found to differ by 4.844 eV, so the virtual energies of the latter configuration have been shifted upward to establish this difference, instead of being represented relative to the HOMO. The relative energies of various $2p_{3/2}^{-1}5f$ excited states are then taken relative to the energy of $2p_{3/2}^{-1}5f_{xyz}^1$, while those of the various $2p_{3/2}^{-1}6d$ excited states are taken relative to the energy of $2p_{3/2}^{-1}6d_{xy}^1$. Table 1 summarizes the energies and relative intensities of the transitions to the various virtual spinors using this $2p_{3/2}^{-1}(5f/6d)^1$ model and compares these to the equivalent relative energies for the fully ionized case ($2p_{3/2}^{-1}$). The symmetry labels used in Table 1 are not those of the D'_{4h} double group used in Figure 3, rather they are intended to indicate the principal orbital parentage, either in $D_{\infty h}$ or D_{4h} (Table 3).

3.3. Comparison between ADF and Experimental Results.

The results of simulations using the data in Table 4 and a Lorentzian line width of 3.4 eV for 0° and 90° are shown in Figure 6. While the general shape of the L_3-edge spectra appears satisfactory, the dipolar intensity in the calculated parallel polarization is larger than for the calculated perpendicular polarization, which contrasts experimental observation (Figure 1). The dipolar intensity in the parallel polarization is dominated by transitions to $6d\pi$ and $6d\sigma$ orbitals. Eigenvectors show that covalency is small except for $6d\pi$ and $6d\sigma$; the former interacts strongly with both oxygen and chlorine π-orbitals and the latter with oxygen orbitals. To mimic this, the intensity of transitions to these orbitals was reduced by a factor of 0.7 to account qualitatively for the attenuation of their metal character introduced by covalency.

The main features of these simulations agree satisfactorily with the experimental spectra (see Figure 6b and c): higher intensity and lower relative energy position of the spectrum in the 90° versus the 0° geometry. In particular, the relative intensity of the quadrupole allowed transitions to the 5f shell compared to the dipole allowed transitions to the 6d shell is well-reproduced.

The 0.5 eV difference between the absorption maxima in the parallel and perpendicular polarizations using the $(2p_{3/2})^{-1}(5f/6d)^1$ model and including covalence in Figure 6 can be compared to the experimental difference of 0.9 ± 0.1 eV. This difference reflects the fact that the barycenter of the $6d_{xy}$ and $6d_{x^2-y^2}$ orbitals, to which transitions are forbidden in the parallel polarization, lies ~0.6 eV below that of the $6d\pi$ and $6d\sigma$ components. The substantially larger width of the 90° spectrum

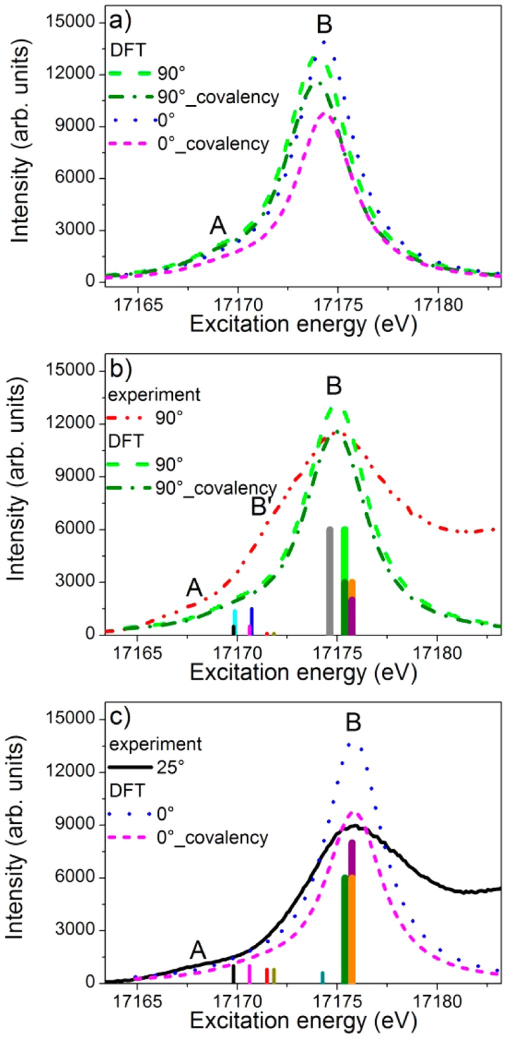

Figure 6. DFT calculated U L_3-edge PD-HR-XANES spectra for the 90° and 0° geometry (a). DFT calculated and experimental U L_3-edge PD-HR-XANES spectra and relative oscillatory strengths for $2p_{3/2} \rightarrow 5f$ (thin bars) and $2p_{3/2} \rightarrow 6d$ transitions (thick bars) for the 90° (b) and 0° geometry (c). The unoccupied orbitals are marked with different colors: $5f\delta_{3/2}$ (black), $5f\phi_{5/2}$ (cyan), $5f\delta_{5/2}$ (magenta), $5f\phi_{7/2}$ (blue), $5f\pi_{1/2}$ (red), $5f\pi_{3/2}$ (dark yellow), $5f\sigma$ (dark cyan), $6d_{xy}$ (gray), $6d_{x^2-y^2}$ (green), $6d\pi_{1/2}$ (olive), $6d_{z^2}$ (purple), $6d\pi_{3/2}$ (orange). For clarity the $2p_{3/2} \rightarrow 5f$ intensities are multiplied by 4 therefore they deviate from the 2.48% $2p_{3/2} \rightarrow 6d$ relative intensity reported in Table 4.

is primarily due to the tetragonal field splitting of the $6d_{xy}$ and $6d_{x^2-y^2}$ orbitals. Indeed, a shoulder can be discerned on the rising edge of the experimental spectrum at about 17172 eV (feature B′), consistent with this description. The simulation does not reproduce well the separation between the barycenters of the 5f and 6d absorption regions: ∼5.2 eV compared to the experimental separation of 7.0 eV (25°)/7.7 eV (90°) (see Table 1). In the perpendicular case, the dominant intensity occurs from transitions to $5f\delta$ and $5f\phi$, which are nearly degenerate and ∼2.5 eV lower in energy than $5f\pi$. These transitions are most likely to be detectable on the low energy side of the intense dipole-allowed transitions to the 6d shell. Indeed, the pre-edge feature of the 90° spectrum is found at −1.5 eV ± 0.1 eV lower energy position compared to the 25° spectrum, whereas the peak area remains similar (Figure 2, Table 1). The limitations of the DFT method are revealed by the calculated value for the excitation energy, 17 623 eV, compared to the experimental value, 17 169 eV, a difference of 2.6%.

Calculations with a hole in the 3d shell give a very similar pattern of energy levels for excitation to 5f, 6d, and ionization (see Supporting Information Table S1). The assignments of the U M_4-edge PD-HR-XANES absorption resonances in section 3.1 are confirmed by ADF (see Table 4 and Supporting Information Table S1). Peak D in the U M_4-edge PD-HR-XANES spectrum for the $\alpha = \alpha_1 + 5°$ $(0 \leq \alpha_1 \leq 45°)$ geometry (see Supporting Information Figure S5) exhibits asymmetric shape, evidence for transitions to $5f\delta$ and $5f\phi$ orbitals with about 0.6 eV energy separation. The ground state calculation with and without spin−orbit interaction yields about 0.1 and 0.8 eV energy separation between $5f\delta$ and $5f\phi$ orbitals, respectively, essentially unaffected by the presence of $3d_{3/2}$ core-hole (see Table 4 and Supporting Information Table S1). $5f\delta_{3/2}$ and $5f\phi_{5/2}$ are nearly degenerate, as well as $5f\delta_{5/2}$ and $5f\phi_{7/2}$. The experimental and theoretical results suggest that spin−orbit interaction is required to reproduce the experimentally observed energy difference.

The integral intensities of the D, E, and F absorption resonances averaged over the U M_4-edge PD-HR-XANES spectra have ratio 5:3.5:1, which deviates from the theoretically predicted 4:2:1. This difference needs to be addressed in future systematic U M_4-edge studies of model powder compounds. Self-absorption effects might also have an influence on peak intensities; therefore, for quantitative analyses, their careful assessment is required. However, in our case at hand such effects do not significantly contribute to our spectra, as comparison to spectra of diluted materials with low U concentration has shown.

In the M_4-edge spectra the oscillatory strength of transitions to δ and ϕ orbitals change significantly (D), whereas the transitions to π (E) and σ (F) orbitals remain very similar within the probed 40° angular range. As reported in Table 4 the relative quadrupole intensities (see Figure 6 b and c) of transitions to π and σ orbitals should increase. This is not observed in the M_4-edge experimental spectra and might be attributed to too small relative intensity changes for 40° change. The contribution of transitions to π and σ orbitals is clearly visible in the L_3-edge spectra as the barycenter of the pre-edge peak shifts to higher energies going from the 90° to the 0° geometry, which confirms that the L_3 and M_4-edge results are consistent.

3.4. FEFF9.6 Calculations. The U L_3-edge PD-HR-XANES spectra calculated with the FEFF9.6 code are shown in Figure 7. The spectra calculated for the 90° or 0° geometry including only dipole allowed $(2p_{3/2} \rightarrow 6d)$ electronic transitions reproduce the overall shape of the experimental spectra well, with exception of absorption resonance A (Figure 7a, b). Feature A gains significant intensity by considering quadrupole transitions $(2p_{3/2} \rightarrow 5f)$ in the calculations. By comparing spectra with the U f- and d-density of states (DOS) in Figure 7 c, it is apparent that f-DOS has strong intensity in this pre-edge region, whereas there is no significant d-DOS contribution. This observation agrees with ADF results and previous studies.[22,25] The d-DOS describes the remaining part of the spectrum well, as expected from dipole selection rules. Note that no polarization dependency is included in the DOS calculations. Comparison to the ADF calculation results allow us to assign feature B′ to electronic $2p_{3/2} \rightarrow 6d_{xy}$ transitions with significant oscillatory strength in the perpendicular

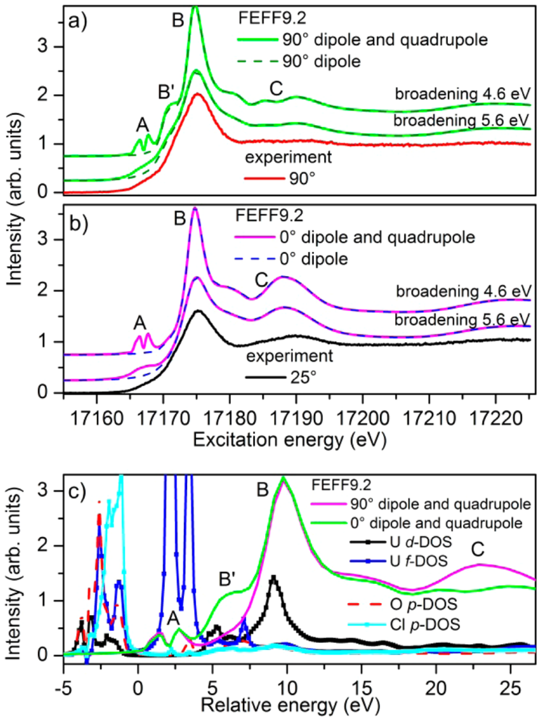

Figure 7. FEFF9.6 calculated with 4.6 and 5.6 eV broadening and experimental U L_3-edge PD-HR-XANES for the 90° (a) and 0° geometry (b); FEFF9.6 calculated U L_3-edge PD-HR-XANES for the 90° and 0° geometry (broadening 4.6 eV) and U, O, Cl DOS (c).

geometry, manifested by an asymmetric shape of the experimental 90° WL. These transitions are not observed in the parallel geometry spectrum shown in Figure 5b, as also found by ADF (Table 1). Feature C gains intensity in the parallel case, which implies ε is directed along the UO_2^{2+} molecule axis. The FEFF9.6 calculations reproduce well the energy positions of all spectral features and their relative intensities by adding 5.6 eV broadening into the simulations to account for both experimental and core−hole lifetime broadening.

4. CONCLUSIONS

Our ADF and FEFF9.6 calculations demonstrate that the pre-edge observed in the experimental U L_3-edge PD-HR-XANES spectra originates mainly from weak $2p_{3/2} \rightarrow 5f$ transitions. Additionally, no electronic transitions to the $6d_{xy}$ orbital are present when ε is aligned with the uranyl moiety. This theoretical result was experimentally confirmed for the first time and is manifested in the experimental U L_3-edge PD-HR-XANES recorded at a 90° geometry (perpendicular relation between uranyl cation and ε) by an asymmetry (feature B′ in Figures 6 and 7), larger area and energy shift to lower energies of the WL; B′ is absent in the 0° PD-HR-XANES.

The low intensity of the broad pre-edge and its overlap with the intense main $2p_{3/2} \rightarrow 6d$ dipole transitions prevent accurate estimation of mixing of ligand with metal *f* orbitals from conventional spectra. The increased energy resolution of HR-XANES allows a pre-edge from the main absorption transitions to be distinguished. Comparison of experimental results with spectra simulated using our ADF calculations with and without the inclusion of covalence, strongly suggests the existence of covalent bonding between the U and the ligands with about 30% mixing of 6dπ and 6dσ with O and Cl valence orbitals. The spin−orbit interaction, taken into account in both ADF and FEFF9.6 codes, mainly introduces splitting of 5fδ, 5fϕ, and 5fπ states and its inclusion is prerequisite to accurate interpretation of U M_4-edge HR-XANES spectra. The comparatively large broadening in U L_3 edge HR-XANES prevents detection of these split f states in the pre-edge region. The FEFF9.6 code is accurate in performing U L_3-edge HR-XANES calculations and reliably reproduces the edge and the post edge regions. Our results should encourage its application in future electronic and geometric structural investigations of actinide materials. On the basis of the example we have provided here, the combination of this as a tool and the HR-XANES technique will increase the degree of accuracy in probing actinide electronic structure in future studies and thereby stimulate development of theoretical codes.

■ ASSOCIATED CONTENT

Ⓢ Supporting Information

Computational details, experimental details, and analyses of U L_3-edge extended X-ray absorption fine structure (EXAFS) spectra, example of a feff.inp used for the FEFF9.6 calculations. This material is available free of charge via the Internet at http://pubs.acs.org.

■ AUTHOR INFORMATION

Corresponding Author

*E-mail: Tonya.Vitova@kit.edu.

Present Address

△M.A.D.: Dalton Nuclear Institute, The University of Manchester, Manchester, M13 9PL, United Kingdom.

Notes

The authors declare no competing financial interest.

■ ACKNOWLEDGMENTS

We acknowledge the Helmholtz Association of German Research Centers for the VH-NG-734 grant and both the Synchrotron light source ANKA and the European Synchrotron Radiation Facility (ESRF) for provision of instrumentation and beamtime. This work is partially funded by the German Federal Ministry of Education and Research (BMBF) under contracts 02NUK020A, 02NUK012A and 02NUK012D. J.J.K. and J.J.R. acknowledge the DOE GrantNo. DE-FG03-97ER45623 and the DOE Computational Materials Science Network for support. K.J. was supported by NSF grant OCI-104805.

■ REFERENCES

(1) Grenthe, I.; Drożdżynński, J.; Fujino, T.; Buck, E.; Albrecht-Schmitt, T.; Wolf, S. Uranium. In *The Chemistry of the Actinide and Transactinide Elements*; Morss, L., Edelstein, N., Fuger, J., Eds.; Springer: Netherlands, 2006; pp 253−698. Denecke, M.; Nolf, W.; Rack, A.; Tucoulou, R.; Vitova, T.; Falkenberg, G.; Abolhassani, S.; Cloetens, P.; Kienzler, B. Speciation of Actinides in Granite Subjected to Tracer Studies. In *Actinide Nanoparticle Research*; Kalmykov, S. N., Denecke, M. A., Eds.; Springer: Berlin, 2011; pp 413−435. Geckeis, H.; Lützenkirchen, J.; Polly, R.; Rabung, T.; Schmidt, M. *Chem. Rev.* **2013**, *113* (2), 1016−1062. Altmaier, M.; Gaona, X.; Fanghänel, T. *Chem. Rev.* **2013**, *113* (2), 901−943. Walther, C.; Denecke, M. A. *Chem. Rev.* **2013**, *113* (2), 995−1015.

(2) Panak, P. J.; Geist, A. *Chem. Rev.* **2013**, *113* (2), 1199−1236.

(3) Barker, T. J.; Denning, R. G.; Thorne, J. R. G. *Inorg. Chem.* **1987**, *26* (11), 1721−1732. Pepper, M.; Bursten, B. E. *Chem. Rev.* **1991**, *91* (5), 719−741. Schreckenbach, G.; Hay, P. J.; Martin, R. L. *J. Comput. Chem.* **1999**, *20* (1), 70−90. Matsika, S.; Pitzer, R. M. *J. Phys. Chem. A* **2000**, *105* (3), 637−645. Kaltsoyannis, N. *Chem. Soc. Rev.* **2003**, *32*

(1), 9–16. Clark, A. E.; Sonnenberg, J. L.; Hay, P. J.; Martin, R. L. *J. Chem. Phys.* **2004**, *121* (6), 2563–2570. Pierloot, K.; van Besien, E. *J. Chem. Phys.* **2005**, *123* (20), -. Réal, F.; Vallet, V.; Marian, C.; Wahlgren, U. *J. Chem. Phys.* **2007**, *127* (21), -. Liu, G.; Deifel, N. P.; Cahill, C. L.; Zhurov, V. V.; Pinkerton, A. A. *J. Phys. Chem. A* **2011**, *116* (2), 855–864. Zhurov, V. V.; Zhurova, E. A.; Stash, A. I.; Pinkerton, A. A. *J. Phys. Chem. A* **2011**, *115* (45), 13016–13023. Tecmer, P.; Bast, R.; Ruud, K.; Visscher, L. *J. Phys. Chem. A* **2012**, *116* (27), 7397–7404. Dau, P. D.; Su, J.; Liu, H.-T.; Huang, D.-L.; Li, J.; Wang, L.-S. *J. Chem. Phys.* **2012**, *137* (6), -. Gomes, A. S. P.; Jacob, C. R.; Real, F.; Visscher, L.; Vallet, V. *Phys. Chem. Chem. Phys.* **2013**, *15* (36), 15153–15162. Schnaars, D. D.; Wilson, R. E. *Inorg. Chem.* **2013**, *52* (24), 14138–14147.

(4) Denning, R. G. *Struct. Bonding (Berlin)* **1992**, *79*, 215–276.

(5) Denning, R. G. *J. Phys. Chem. A* **2007**, *111* (20), 4125–4143.

(6) Spencer, L. P.; Yang, P.; Minasian, S. G.; Jilek, R. E.; Batista, E. R.; Boland, K. S.; Boncella, J. M.; Conradson, S. D.; Clark, D. L.; Hayton, T. W.; Kozimor, S. A.; Martin, R. L.; MacInnes, M. M.; Olson, A. C.; Scott, B. L.; Shuh, D. K.; Wilkerson, M. P. *J. Am. Chem. Soc.* **2013**, *135* (6), 2279–2290.

(7) Templeton, D. H.; Templeton, L. K. *Acta Crystallogr. A* **1982**, *38* (Jan), 62–67.

(8) Hudson, E. A.; Allen, P. G.; Terminello, L. J.; Denecke, M. A.; Reich, T. *Phys. Rev. B* **1996**, *54* (1), 156–165.

(9) Denning, R. G.; Green, J. C.; Hutchings, T. E.; Dallera, C.; Tagliaferri, A.; Giarda, K.; Brookes, N. B.; Braicovich, L. *J. Chem. Phys.* **2002**, *117* (17), 8008–8020.

(10) Fonseca Guerra, C.; Snijders, J. G.; te Velde, G.; Baerends, E. J. *Theor. Chem. Acc.* **1998**, *99* (6), 391–403. te Velde, G.; Bickelhaupt, F. M.; Baerends, E. J.; Fonseca Guerra, C.; van Gisbergen, S. J. A.; Snijders, J. G.; Ziegler, T. *J. Comput. Chem.* **2001**, *22* (9), 931–967.

(11) Rehr, J. J.; Kas, J. J.; Vila, F. D.; Prange, M. P.; Jorissen, K. *Phys. Chem. Chem. Phys.* **2010**, *12* (21), 5503–5513.

(12) Ohwada, K. *Spectrochim Acta A* **1975**, *31* (7), 973–977. Hall, D.; Rae, A. D.; Waters, T. N. *Acta Crystallogr.* **1966**, *20*, 160–&.

(13) Glatzel, P.; Bergmann, U. *Coord. Chem. Rev.* **2005**, *249* (1–2), 65–95.

(14) Baerends, E. J. *ADF Program System*, version 2000.02; Vrije Universiteit: Amsterdam, 2000.

(15) Baerends, E. J.; Ellis, E. G.; Ros, P. *Chem. Phys.* **1973**, *2*, 41. te Velde, B.; Baerends, E. J. *J. Comput. Phys.* **1992**, *99*, 84.

(16) van Lenthe, E.; van Leeuwen, R.; Baerends, E. J.; Snidgers, J. G. *Int. J. Quantum Chem.* **1996**, *57*, 281. van Lenthe, E.; Snidgers, J. G.; Baerends, E. J. *J. Chem. Phys.* **1996**, *105*, 6505.

(17) Vosko, S. H.; Wilk, L.; Nusair, M. *Can. J. Phys.* **1980**, *58*, 1200.

(18) Becke, A. D. *Phys. Rev. A* **1988**, *38*, 3098.

(19) Perdew, J. P. *Phys. Rev. B* **1986**, *33*, 8822.

(20) Vitova, T.; Denecke, M. A.; Göttlicher, J.; Jorissen, K.; Kas, J. J.; Kvashnina, K.; Prüßmann, T.; Rehr, J. J.; Rothe, J. *J. Phys.: Conf. Ser.* **2013**, *430* (1), No. 012117.

(21) de Groot, F. M. F.; Krisch, M. H.; Vogel, J. *Phys. Rev. B* **2002**, *66* (19), No. 195112.

(22) Vitova, T.; Kvashnina, K. O.; Nocton, G.; Sukharina, G.; Denecke, M. A.; Butorin, S. M.; Mazzanti, M.; Caciuffo, R.; Soldatov, A.; Behrends, T.; Geckeis, H. *Phys. Rev. B* **2010**, *82* (23), No. 235118.

(23) Petiau, J.; Calas, G.; Petitmaire, D.; Bianconi, A.; Benfatto, M.; Marcelli, A. *Phys. Rev. B* **1986**, *34* (10), 7350–7361.

(24) Fillaux, C.; Berthet, J. C.; Conradson, S. D.; Guilbaud, P.; Guillaumont, D.; Hennig, C.; Moisy, P.; Roques, J.; Simoni, E.; Shuh, D. K.; Tyliszczak, T.; Castro-Rodriguez, I.; Den Auwer, C. *C. R. Chim.* **2007**, *10* (10–11), 859–871.

(25) Walshe, A.; Prussmann, T.; Vitova, T.; Baker, R. J. *Dalton Trans.* **2014**, *43* (11), 4400–4407.